myjournal manuscript No.
(will be inserted by the editor)

The effect of sudden permeability changes in porous media filling box flows

Chunendra K. Sahu · **M. R. Flynn**

Received: date / Accepted: date

Abstract We report upon experimental and analytical investigations of filling box flows in non-uniform porous media characterized by a sudden change of permeability. The porous medium consists of two layers separated by a horizontal permeability jump and is initially filled with light ambient fluid. A line source located at the top of the upper layer supplies dense contaminated fluid that falls towards the bottom of the domain. Two configurations are studied, i.e. a low permeability layer on top of a high permeability layer and vice-versa. In the former scenario, the flow dynamics are qualitatively similar to the case of a uniform porous medium. Thus the analytical formulation of Sahu & Flynn (*J. Fluid Mech.*, vol. 782, 2015, pp. 455–478) can be adopted to compute the parameters of interest, e.g. the plume volume flux. In the latter scenario, the flow dynamics are significantly different from those of the uniform porous medium case; after reaching the permeability jump, some fraction of the dense plume propagates horizontally as a pair of oppositely-directed interfacial gravity currents. Meanwhile, the remaining fraction of the plume flows downwards into the lower layer where it accumulates along the bottom boundary in the form of a deepening layer of discharged plume fluid. Depending on the permeability ratio of the upper and lower layers and the source conditions, the gravity currents may become temporarily arrested after travelling some finite horizontal length. An analytical prediction for this so-called run-out length is derived, motivated, in part, by the immiscible analysis of Goda & Sato (*J. Fluid Mech.*, vol. 673, 2011, pp. 60–79). Finally, a prediction of the filling box time, consisting of the time required to fill the control volume up to the point of contaminated fluid overflow, is made. These predictions are compared with analogue experimental measurements. Generally positive agreement is found when the higher permeability layer is located below the lower permeability layer. In the opposite circumstance, the agreement is conditional. If the run-out length of the gravity current is less than the horizontal dimensions of the control volume (or tank in case of the experiments), the agreement is good. By contrast, when the

C. K. Sahu
E-mail: chunendra@ualberta.ca
Dept. of Mechanical Engineering and Inst. for Geophysical Research, University of Alberta, T6G 1H9, Canada

M. R. Flynn
E-mail: mrflynn@ualberta.ca
Dept. of Mechanical Engineering and Inst. for Geophysical Research, University of Alberta, T6G 1H9, Canada

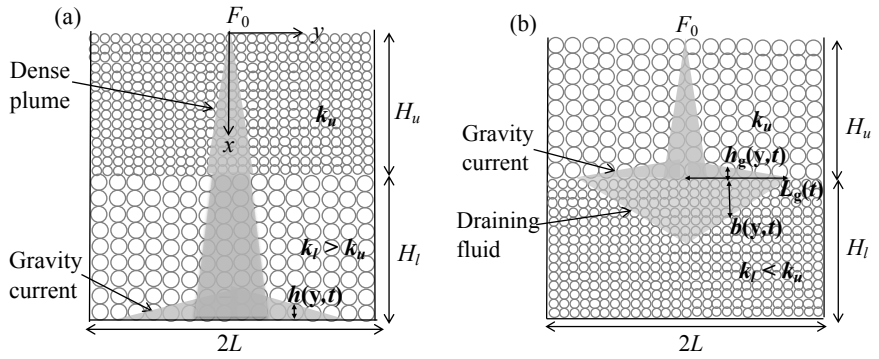

Fig. 1: Filling box flows in two-layer porous media: (a) $k_u/k_\ell < 1$, (b) $k_u/k_\ell > 1$.

run-out length is large, comparatively poor agreement may be realized: in spite of the higher density of the contaminated fluid, it may occupy the entirety of the upper layer before filling the lower layer.

1 Introduction

Filling box flows arise in closed or ventilated control volumes, often rectilinear or cylindrical in shape, where the flow is buoyancy-driven and originates from a compact hot or cold source. Though first developed in the context of turbulent buoyant convection ("plumes in rooms"), porous media filling box-type models have recently gained popularity because of their application to various geophysical phenomena, e.g. leakage of contaminants from landfills and waste piles (Moradi and Flynn, 2017) and geothermal energy recovery (Dudfield and Woods, 2012). In that context, Roes et al (2014) studied the particular impact of fissure drainage on the long time behaviour of a porous media filling box flow. Thereafter, and motivated by the analogue problem investigated by Baines and Turner (1969), Sahu and Flynn (2015, 2016) studied filling box flows in closed rectilinear and axisymmetric geometries and presented analytical solutions for the associated flow dynamics consisting of a descending plume and plume outflow along the impermeable boundaries. An important simplification applied in each of the above studies is that they consider uniform porous media consisting of a constant porosity, ϕ, and permeability, k. In real geophysical scenarios, however, ϕ and k typically vary in space and can be considered constant only within localized, and often quite thin, geological strata. Although the effects of variations in ϕ and k have been studied previously in the context of gravity currents (Pritchard et al, 2001; Pritchard and Hogg, 2002; Goda and Sato, 2011; Huppert et al, 2013), these effects remain comparatively unexplored in the context of filling box flows. Therefore in the present investigation, we study nonuniform porous media filling box flows paying particular attention to the effects of a sudden change of permeability between adjacent horizontal layers.

Figure 1 shows schematics of the flow and flow domain. A rectilinear control volume (or tank) consists of two different porous media layers and is closed along all but the upper boundary. This upper boundary in turn contains a source of negatively-buoyant fluid that falls in the form of a laminar plume. We invoke the Boussinesq approximation, valid for modest density differences, according to which our results apply equally well to a buoyant

rising plume. After falling a vertical distance H_u, the plume encounters the permeability jump between the upper and lower layers and thereafter its motion, and the consequent dispersion of contaminated fluid, depends upon the permeability, k_ℓ, of the lower layer. If $k_\ell > k_u$ where k_u is the permeability of the upper layer, then plume fluid easily descends to the bottom of the control volume (figure 1 a). In contrast, when $k_\ell < k_u$, the plume fluid splits in two with some fraction flowing horizontally in the form of a "leaky" interfacial gravity current and the remaining fraction propagating directly into the lower layer.

Predicting the fraction of the plume that detrains along the permeability jump as a function of k_u/k_ℓ and the source conditions is a complicated task. Nonetheless, helpful insights into the flow behaviour can be realized using comparatively simple formulas based, in part, on existing plume models. Such models enjoy a rich history dating back to Wooding's seminal paper wherein he derived an analytical solution for plumes in a Darcy regime, i.e. with Reynolds number $\mathrm{Re} = \dfrac{d_0 U}{\nu} \leq \mathscr{O}(10)$, where d_0 is the mean grain diameter, U is the average transport velocity, and ν is the kinematic viscosity. Wooding (1963) further assumed a small Péclet number, i.e. $\mathrm{Pe} = \dfrac{d_0 U \tau}{D_d} \ll \mathscr{O}(1)$, where D_d is the molecular diffusion coefficient and τ is the flow path tortuosity. For a non-Darcy flow regime, i.e. when $\mathrm{Re} > \mathscr{O}(10)$, Wooding's study was subsequently extended by Chen and Ho (1986) and Lai (1991) who respectively considered cases where $\mathrm{Pe} \ll \mathscr{O}(1)$ and $\mathrm{Pe} \gg \mathscr{O}(1)$. More recently, Sahu and Flynn (2015) returned to Wooding's Darcy flow formulation but assumed $\mathrm{Pe} \gg \mathscr{O}(1)$. Following this line of inquiry, and consistent with the experiments to be described in section 2, we likewise consider the flow to be in a Darcy regime with $\mathrm{Pe} \gg \mathscr{O}(1)$.

As indicated schematically in figure 1 b, fluid detrained from the plume at the permeability jump (and also at the bottom of the control volume) form gravity currents that propagate left and right. Gravity current flow through a free medium but over a porous base has been studied by several researchers e.g. Thomas et al (1998), Ungarish and Huppert (2000), Acton et al (2001) and Spannuth et al (2009). The problem at hand draws insights from these helpful investigations but more properly falls into the category of interfacial gravity current flow in porous medium over a low permeability substrate, which was first studied analytically by Pritchard et al (2001). They assumed a constant volume flux source and a lower layer thickness that was much less than the interfacial gravity current height. Pritchard et al (2001) found that, after reaching a certain horizontal distance, the interfacial gravity current stopped moving forward at which point the influx from behind the gravity current head was balanced by drainage along the gravity current underside. Extending this investigation to lower (and upper) layers of infinite depth, Goda and Sato (2011), considering immiscible fluids, presented a numerical solution that specified the forward propagation of the interfacial gravity current and the downward motion of the draining fluid as functions of time as well as parameters such as the permeability ratio, k_u/k_ℓ. Consistent with Pritchard et al (2001), Goda and Sato (2011) found that the current length approaches some maximum value in the long time limit, $t \to \infty$. This maximum length is given by

$$\check{L}_g = \frac{q\nu}{k_\ell g'} \,. \tag{1}$$

Here ν is the kinematic viscosity and q and $g' = g\dfrac{\rho_1 - \rho_\infty}{\rho_\infty}$ are respectively the interfacial gravity current volume flux per unit length and reduced gravity. Moreover ρ_1 and ρ_∞ are the respective fluid densities of the interfacial gravity current and ambient. Because the present investigation considers miscible fluids and a confined volume, in section 3.2 we employ a

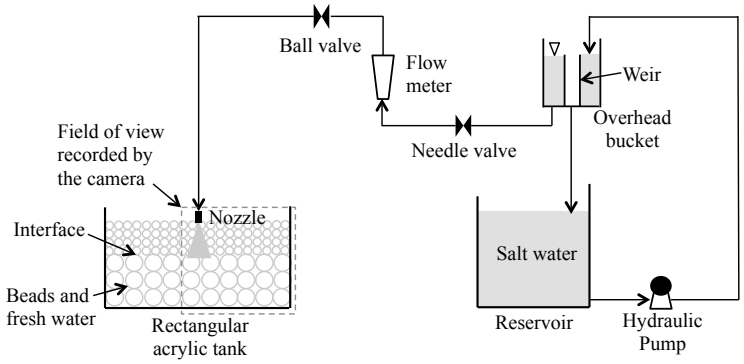

Fig. 2: Schematic of the experimental setup.

similar methodology to Goda and Sato (2011) but with some essential modifications, primarily to allow for mixing between the interfacial gravity current and ambient fluids.

Our model predictions are compared against analogue laboratory data. Of particular interest are the gravity current run-out length, measured in the lower layer, and the timescales required for the contaminated fluid to reach the point of overflow. These estimates are made with respect to the permeability and height ratios of the lower to upper layers and the source volume flux and reduced gravity.

The rest of the manuscript is organized as follows: section 2 outlines the experimental setup and procedure, image post-processing details and qualitative observations. Corresponding model equations are developed and discussed in section 3 and a comparison with laboratory data is given in section 4. Finally, section 5 presents conclusions and defines topics for future work.

2 Experimental technique

2.1 Laboratory set-up and experiments

A schematic of the experimental set-up is shown in figure 2. A transparent acrylic tank 88.9 cm long $\times$ 7.6 cm wide $\times$ 50.8 cm tall was filled with tap water of density 0.998 g/cm^3 and two layers of Potters Industries A Series Premium glass beads. We considered three different sets of experiments where the ratio of upper (H_u) to lower (H_ℓ) layer depth was 0.5, 1.0 or 2.0. The total depth of both layers, $H = H_u + H_\ell$, was either 36 cm or 40 cm. The beads measured either 0.1 cm, 0.3 cm or 0.5 cm in diameter, which yielded permeability ratios, k_u/k_ℓ, of 0.04, 0.11, 0.36, 2.8, 9.0 and 25.0. Permeabilities were calculated using the relationship originally derived by Rumpf & Gupte, and employed in the experimental investigations of Acton et al (2001), Lyle et al (2005) and others, such that $k = \dfrac{d^2\phi^{5.5}}{5.6}$ where d is the bead diameter and ϕ is the porosity. Following Happel and Brenner (1991), we assume $\phi = 0.38$ corresponding to randomly distributed spherical beads.

The plume source fluid consisted of salty water to which Procion MX Cold Water dye had been added for purposes of flow visualization. Before the start of an experiment, this fluid was mixed in a 100 L reservoir (see figure 2). The dense fluid in question was then

supplied to the rectangular acrylic tank using a hydraulic pump, overhead bucket, flowmeter, flow valves and a line nozzle. The overhead bucket had a cylindrical internal weir which helped to maintain a constant source pressure. A Gilmont GV-2119-S-P flowmeter was used to measure the flow rate, which was adjusted using ball and needle valves. The last component of the flow system before dense fluid reached the tank was a line nozzle of discharge area $A_{\text{nozzle}} = 2.8\,\text{cm}^2$, which was fitted at the top centre of the tank and spanned the tank width. The nozzle, which is further described in Roes (2014), was designed so as to minimize the momentum of the exiting fluid.

Experimental images were captured every 60 s using a Canon Rebel EOS T2i 18.0 PM camera fitted with an 18-55 mm IS II zoom lens. The experiments usually lasted between 1 h and 3 h depending upon the flow rate and permeability ratio. Thus, over the course of a single experiment, roughly 60 to 200 images were recorded. Because of the symmetric nature of the flow, and so as to reduce parallax errors, only one half of the experimental tank was visualized. The tank was backlit using a 3M 1880 overhead projector and its backside was covered with tracing paper, which acted to diffuse the light from this projector.

As summarized in Appendix A, a total of 50 experiments were performed where we regard k_u/k_ℓ, H_u/H_ℓ, the plume source volume flux, Q_0, and reduced gravity, g'_0, as independent variables. Here $g'_0 = g\dfrac{\rho_0 - \rho_\infty}{\rho_\infty}$ where ρ_0 is the source fluid density.

2.2 Experimental images

Experimental images were post-processed using Matlab. Images were first cropped then converted from RGB to grey-scale. They were then subtracted from a reference image taken just before the beginning of an experiment. This subtraction operation helped to highlight differences between ambient (clear) fluid and dense (dyed) fluid whether within the plume or discharged in the form of a deepening layer along the bottom of the tank. Regions uncontaminated by dense fluid therefore had an intensity of zero and appear as black in the figures to follow.

2.2.1 Low permeability layer on top of high permeability layer: experiments with $k_u/k_\ell < 1$

Figure 3 shows post-processed experimental images for all six permeability ratios considered in this study. In each case, images are collected 1000 s after the descending plume is "switched on." For the first three cases where $k_u/k_\ell < 1$, the flow behaviour is qualitatively similar to the case of a uniform porous medium (Sahu and Flynn, 2015, figure 6). The dense plume flows with comparative ease into the lower layer, and subsequently produces a pair of laterally propagating gravity currents, followed by a deepening layer of discharged plume fluid. The depth of this lower layer is described in terms of the average elevation of the "first front," the fluid interface separating the dense lower layer from the ambient upper layer. First front elevations were determined using the maximum gradient algorithm developed by Roes (2014) and subsequently employed by Roes et al (2014) and Sahu and Flynn (2015). By measuring the first front elevation and its time derivative, it was straightforward to estimate the advection speed as a function of time. Consequently the times required by the first front to reach the permeability jump and then the nozzle were calculated.

Lyu and Woods (2016), in their experimental investigation of buoyant plumes in porous media, found that if the ratio of the injection speed to the buoyancy rise speed was large, the plume exhibited a finger-dominated head. Fingers were also observed in select experiments

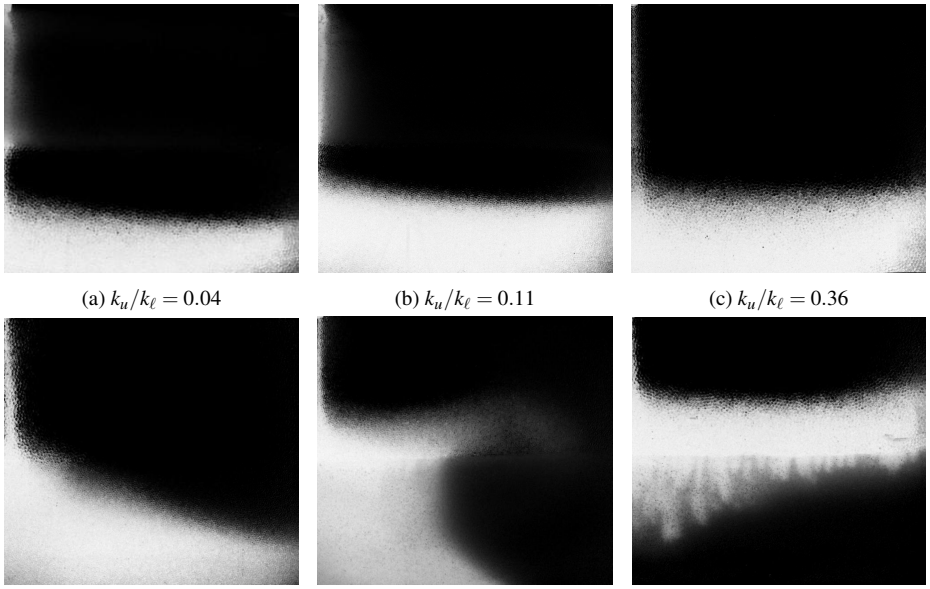

(a) $k_u/k_\ell = 0.04$ (b) $k_u/k_\ell = 0.11$ (c) $k_u/k_\ell = 0.36$

(d) $k_u/k_\ell = 2.8$ (e) $k_u/k_\ell = 9.0$ (f) $k_u/k_\ell = 25.0$

Fig. 3: Sample images of experiments with $Q_0 = 0.75$ cm^3/s, $g'_0 = 80.0$ cm/s^2 and $H_u/H_\ell = 1.0$ at $t = 1000$ s. Permeability ratios are as indicated. In sequence, the images belong respectively to Experiments 19, 22, 27, 31, 35 and 40 from table 3, Appendix A. The field of view for each image measures 44 cm long $\times$ 40 cm tall.

from the present study, i.e. when $k_u/k_\ell < 1$ with an upper layer bead diameter of 0.1 cm and a comparatively large (small) source volume flux (reduced gravity). However, the fingers disappeared relatively quickly and the plume thereafter took a form similar to that shown in the upper layer of Figure 3 d. By experimental measurement, we found that the timescale associated with the disappearance of the fingers was much smaller than the filling box time. Therefore, in the theoretical formulation of section 3.1 we shall neglect this fingering effect.

2.2.2 High permeability layer on top of low permeability layer: experiments with $k_u/k_\ell > 1$

In cases where $k_u/k_\ell > 1$ (i.e. figures 3 d,e,f), we observe qualitatively different flow dynamics from cases where $k_u/k_\ell < 1$. To wit, some fraction of the plume detrains along the interface and forms a pair of (primary) gravity currents that propagate in the tank interior. The remaining fraction of the plume fluid drains down into the lower layer and eventually reaches the tank bottom where it ultimately forms a pair of secondary gravity currents, for which the draining fluid sets influx conditions (see figure 3 e). The immediate penetration of the dense fluid into the lower layer after reaching the permeability jump stands in contrast to the study of Huppert et al (2013). In their investigation of gravity currents in layered porous media, dense fluid was injected from the bottom. Due to the opposing effects of the gravity and inertia, the dense fluid penetrated into the upper layer either after a time delay or not at all.

As k_u/k_ℓ increases, so too does the relative flow resistance in the lower layer and the fraction of plume fluid detrained along the permeability jump. The fluid that comprises

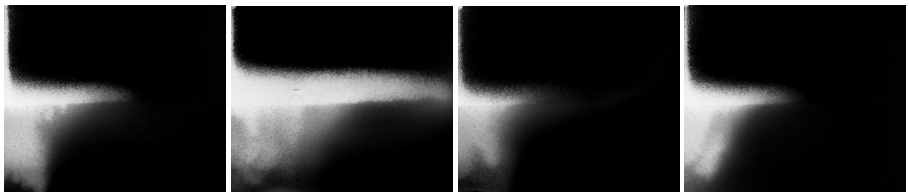

(a) $Q_0 = 0.25$ cm^3/s, $g_0' = 20.0$ cm/s^2, $t = 1400$ s

(b) $Q_0 = 0.75$ cm^3/s, $g_0' = 20.0$ cm/s^2, $t = 1750$ s

(c) $Q_0 = 0.25$ cm^3/s, $g_0' = 80$ cm/s^2, $t = 850$ s

(d) $Q_0 = 0.75$ cm^3/s, $g_0' = 80$ cm/s^2, $t = 400$ s

Fig. 4: Sample images of experiments with $k_u/k_\ell = 9.0$ and $H_u/H_\ell = 1.0$ at the approximate time instants when the draining fluid first reaches the lower impermeable boundary. In sequence, the images belong respectively to Experiments 32, 33, 34 and 35 from table 3, Appendix A. The field of view for each image measures 44 cm long $\times$ 40 cm tall.

this intermediate gravity current can only travel along the permeability jump for so long, however. Once the front travels a horizontal distance $\check{L}_g$, the volume flux of fluid that drains from the gravity current underside matches that detrained from the plume at the level of the permeability jump, H_u. Consistent with the above remarks, $\check{L}_g$ increases with k_u/k_ℓ. Figure 3 f shows that when the permeability ratio is large, i.e. $k_u/k_\ell = 25$, $\check{L}_g$ exceeds the tank half-length, L. In this case, the primary gravity currents reach the sidewalls and start advecting upward well before the lower layer is filled with contaminated fluid. By the time of control volume overflow, therefore, only a small amount of dense fluid has permeated into the lower layer via Rayleigh-Taylor-type fingering (Saffman and Taylor, 1958; Homsy, 1987; Drazin and Reid, 2004).

Because the inflow conditions for the primary gravity currents are prescribed by the outflow conditions of the plume at the permeability jump, the primary gravity current behaviour also depends on the source parameters, i.e. Q_0 and g_0', as well as k_u/k_ℓ and H_u/H_ℓ. Consistent with (1), figure 4 shows that L_g, defined in figure 1 b, increases with increasing Q_0 and decreasing g_0'. For fixed Q_0, larger L_g (and hence $\check{L}_g$) signifies a smaller fraction of plume fluid propagating into the lower, less permeable layer.

The panels of figures 3 and 4 confirm that the pixel intensity, and therefore the density, of the primary gravity current is typically larger than that of the fluid that has drained into the lower layer. The obvious implication is that draining is associated with the entrainment, over a broad horizontal distance, of ambient fluid from below the permeability jump. Appendix B outlines an experimental methodology for estimating the amount of entrainment, expressed as the ratio of densities of contaminated fluid above and below this jump.

2.2.3 Horizontal time series (HTS) for measuring gravity current propagation

Post-processed images were assembled to make movies using Matlab's `immovie` command. Horizontal time series (HTS) images of the type shown in figure 5 d,e,f were then constructed. They show the time variation of pixel intensity along a particular horizontal line within the field of view. In the HTS images, light and dark regions correspond to plume and ambient fluid, respectively. The boundaries between the light and dark regions therefore denote the front position of the primary (figure 5 d) and secondary (figure 5 f) gravity currents

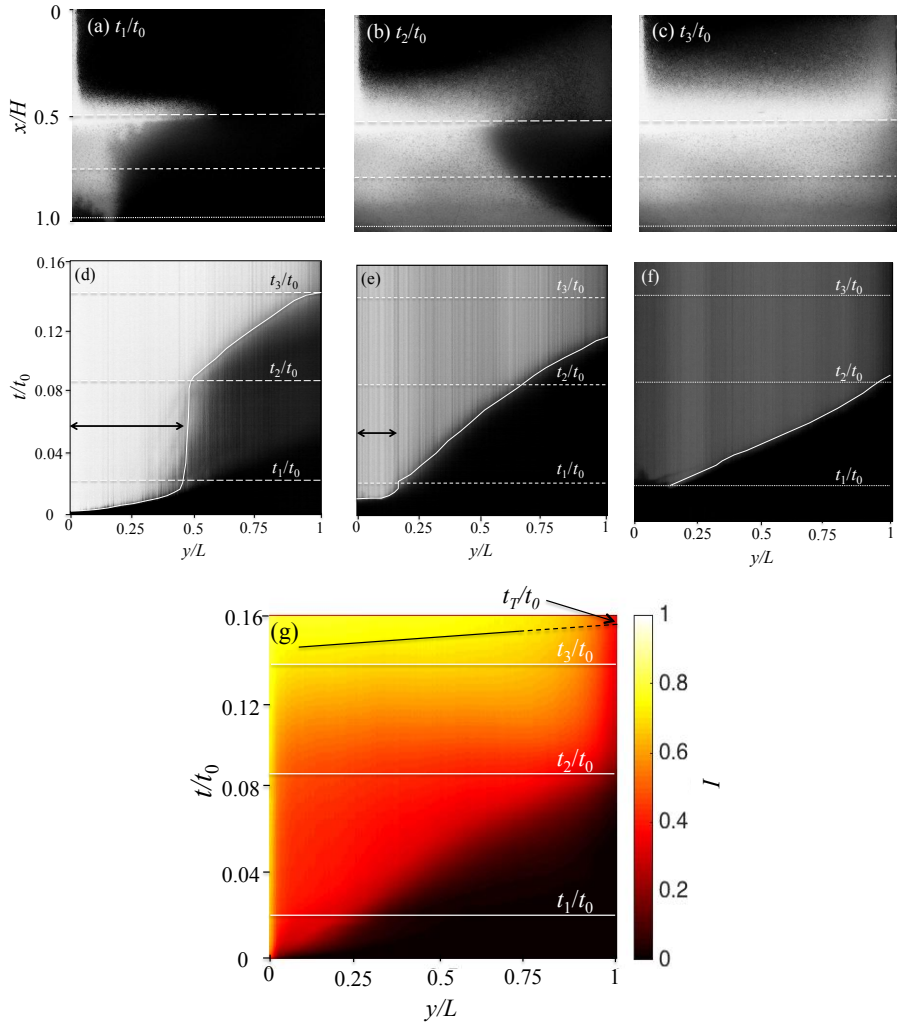

Fig. 5: [Colour online] Examples of horizontal (HTS) and composite (CTS) time series images. HTS images are collected along the permeability jump (panel d corresponding to the long-dashed lines in panels a, b and c), at a depth $H_\ell/2$ below the permeability jump (panel e corresponding to the dashed lines in panels a, b and c) and close to the bottom of the tank (panel f corresponding to the dotted lines in panels a, b and c). The double-headed arrows in panels d and e represent the run-out lengths as measured above and below the permeability jump. The horizontal lines in panel g correspond to the column-wise average intensities of the images in panels a, b and c. On the other hand, the sloping line gives, by extrapolation to the vertical axis, a prediction of the filling box time. The associated timescale t_0 is defined in (2). Images belong to Experiment 32 from table 3, Appendix A, for which the experimental parameters read $Q_0 = 0.25\ \mathrm{cm}^3/\mathrm{s}$, $g_0' = 20.0\ \mathrm{cm}/\mathrm{s}^2$, $k_u/k_\ell = 9.0$ and $H_u/H_\ell = 1.0$.

against time. In figure 5, time is non-dimensionalized by the residence time, t_0, where

$$t_0 = \frac{2\phi\Lambda LH}{Q_0}. \tag{2}$$

Here Λ is the width of the line nozzle.

Panel d shows that the primary gravity current is first apparent shortly after $t = 0$ when the plume is switched on. (Note that for the quantitative analysis to be presented in section 3, we assume $t = 0$ when the dense plume first reaches the lower impermeable boundary or the permeability jump, for $k_u/k_\ell \leq 1$ and $k_u/k_\ell > 1$, respectively). Until the time instant, t_1, when the draining fluid first reaches the bottom boundary, the primary gravity current propagates with a nearly-constant velocity, which later drops to a much smaller value as L_g reaches $\check{L}_g$. The gravity current then maintains roughly the same length $\check{L}_g$ until $t = t_2$, i.e. when the secondary gravity current, formed just after t_1, reaches the right sidewall. Discharged plume fluid then steadily accumulates in the lower layer and the primary gravity current again advances along the permeability jump. Finally at $t = t_3$ the lower layer becomes completely filled with contaminated fluid.

To experimentally measure $\check{L}_g$, we consider the flow dynamics only until t_1, i.e. when the flow is not yet influenced by the finite boundaries of the experimental tank. From figures 5 d and 5 e, and in contrast to figure 2 of Goda and Sato (2011), we find that experimental estimates for $\check{L}_g$ are different, i.e. $\check{L}_g/L \simeq 0.4$ or 0.2, respectively, depending on whether measurements are made immediately above or at some distance below the permeability jump. For purposes of comparing the measured and predicted values of $\check{L}_g$ in section 4, we restrict attention to laboratory estimates derived from below the permeability jump, i.e. from figures such as figure 5 e. The rationale for this choice shall become obvious in sections 3.2 and 4.

2.2.4 Composite time series (CTS) for measuring filling box time

In experiments where $k_u/k_\ell < 1$, a single sharp nearly-horizontal boundary appears between the ambient fluid and that discharged from the plume (see figures 3 a,b,c). It is then straightforward to measure the time required for this first front to reach the point of overflow. However, when $k_u/k_\ell > 1$, figures 3 d,e,f suggest a more convoluted boundary between ambient and contaminated fluid. Because it is oftentimes difficult to unambiguously identify a first front or to measure its vertical velocity from snapshot images, we choose instead to focus attention on a composite time series (CTS). The algorithm for constructing these images is similar to that of section 2.2.3 but replaces, for each time instant, the intensity at a particular pixel with the column-average pixel intensity in the interval $0 < x < H$ (Nicholson and Flynn, 2015). A sample CTS image is shown in figure 5 g. The horizontal lines labeled as t_1/t_0, t_2/t_0 and t_3/t_0 correspond to the snapshot images shown in panels (a), (b) and (c), respectively. The intensity index, I, which appears in the colorbar on the right hand side of the CTS image, and which ranges from 0 to 1, is a surrogate for the fraction of discharged plume fluid contained within a particular column of pixels. From (3.1) of Shin et al (2004), and assuming again that the fluid density scales in proportion to dye concentration, the formula for I reads

$$I(y,t) = \frac{1}{H}\int_0^H \frac{\rho(y,x,t) - \rho_\infty}{\rho_0 - \rho_\infty}\,\mathrm{d}x, \tag{3}$$

where $\rho(y,x,t)$ is the fluid density at any location (y,x) for a particular time, t. Thus, $I = 0$ or 1 indicates, respectively, the presence of only ambient fluid or only source fluid. The latter value is, of course, never realized: because of the entrainment of ambient fluid into the plume, I remains strictly less than unity.

Once the dense fluid reaches the point of overflow, the time rate of increase in the average fluid density becomes much smaller than at early times. Therefore, (3) suggests that at large times the image intensity I should become nearly time-independent; figure 5 g indeed displays this behaviour. (For the region close to the sidewall i.e. $y/L \simeq 1$, the lower image intensity is due to sidewall effects, which allow light from the projector to enter the tank without first passing through those beads adjacent to the back surface of the tank.) In figure 5 g the sloping line shows the times beyond which the time rate of change of pixel intensity becomes suitably small. Meanwhile the dashed line indicates the extension of this solid black line to the point $y/L = 1$. This point of intersection defines the time for overflow, which we label as t_T.

3 Theoretical development

For both $k_u/k_\ell < 1$ and $k_u/k_\ell > 1$, we proceed initially by considering equations that employ dimensional parameters. However, towards the ends of sub-sections 3.1 and 3.2 the filling box times are derived in dimensionless form such that the formulas can be applied to problems spanning a broad range of length scales.

Over $0 < x \leq H_u$, the dense plume behaves like in uniform porous medium and we can therefore use the formulas presented in Sahu and Flynn (2015) for estimating key parameters of interest, i.e. the plume volume flux, $Q(x)$, and reduced gravity, $g'(x)$, averaged over the plume cross-section. The associated equations respectively read

$$Q(x) = \left[\left(\frac{16F_0k_u\Lambda}{\pi\nu}\right)^2 \alpha\phi_u(x+x_0)\right]^{1/4}, \quad g'(x) = \left[\left(\frac{\pi F_0\nu}{16k_u\Lambda}\right)^2 \frac{1}{\alpha\phi_u(x+x_0)}\right]^{1/4}. \quad (4)$$

Here, F_0 is the source buoyancy flux, Λ is the line source width, ν is the fluid viscosity, ϕ_u is the porosity of the upper layer and $0.01 \leq \alpha \leq 1.0$ cm is the dispersivity constant (Delgado, 2007). Moreover, Sahu and Flynn (2015) measured α experimentally and found it to equal 0.015 cm when $\mathrm{Re} \leq \mathscr{O}(10)$ and $\mathrm{Pe} \gg \mathscr{O}(1)$. Furthermore, x_0 represents a virtual origin correction that accounts for the finite source volume flux, $Q_0\,(>0)$, of the (non-ideal) plume; x_0 is given by

$$x_0 = \frac{1}{\alpha\phi_u}\left(\frac{\pi\nu}{16F_0k_u\Lambda}\right)^2 {Q_0}^4. \quad (5)$$

From (4), we can easily calculate the volume flux, Q_u, and mean reduced gravity, g'_u, of the plume at the permeability jump by setting $x = H_u$. The values of Q_u and g'_u specify the inflow conditions for the lower layer plume and the primary gravity currents, the latter of which appear only when $k_u/k_\ell > 1$.

3.1 Permeability ratio $k_u/k_\ell < 1$

When the dense plume enters a lower layer having permeability $k_\ell > k_u$, the qualitative nature of the (primarily vertical) flow remains the same. To describe the lower layer plume quantitatively, we need to introduce a second virtual origin, x_u, whose magnitude depends on Q_u, i.e.

$$x_u = \frac{1}{\phi_\ell\alpha}\left(\frac{\pi\nu}{16F_0k_\ell\Lambda}\right)^2 {Q_u}^4 = \frac{\phi_u}{\phi_\ell}\left(\frac{k_u}{k_\ell}\right)^2 (H_u + x_0). \quad (6)$$

The second equality above is obtained by incorporating the mathematical expression for Q_u.

Now by adapting (4) and replacing k_u, ϕ_u and x_0 with k_ℓ, ϕ_ℓ and x_u, respectively, we can predict the plume volume flux and reduced gravity as functions of x in the lower layer. Thus

$$Q(x) = \left[\left(\frac{16F_0k_\ell\Lambda}{\pi\nu}\right)^2 \alpha\phi_\ell(x-H_u+x_u)\right]^{1/4},$$
$$g'(x) = \left[\left(\frac{\pi F_0\nu}{16k_\ell\Lambda}\right)^2 \frac{1}{\alpha\phi_\ell(x-H_u+x_u)}\right]^{1/4} \quad \text{for} \quad H_u < x \le H\,. \tag{7}$$

Here $H = H_u + H_\ell$ is the control volume height. These results can easily be extended to calculate Q_H and g'_H, the respective values of the plume volume flux and reduced gravity at the bottom of the control volume, by setting $x = H$.

After the dense plume reaches this bottom boundary, its subsequent horizontal motion can be described using the equations for gravity current flow through a porous medium. Employing the results of Sahu and Flynn (2015), which are themselves based on the seminal analysis of Huppert and Woods (1995), it can be shown that the gravity current front speed is given by

$$v_g = \frac{2\lambda}{3}\left(\frac{F_0k_\ell}{2\Lambda\nu\phi_\ell t}\right)^{1/3}. \tag{8}$$

Here $\lambda = 2.046$ is the dimensionless gravity current length (Huppert and Woods, 1995; Sahu and Flynn, 2015). (Note that the value of λ presented in the former article is 1.481, which corresponds to $\phi = 1.0$ for Hele-Shaw-type experiments, whereas $\lambda = 2.046$ in the current investigation where, by assumption, $\phi = 0.38$.) We assume that the time scale associated with plume flow is much smaller than that of either the horizontal motion of the gravity current or the vertical motion of the first front, the latter of which is considered below. This assumption is valid provided $L/H \ge \mathcal{O}(1)$. On this basis, $t = 0$ corresponds to the time instant when the dense plume first reaches the bottom of the control volume. Using (8), the time required for the gravity current to reach the sidewall can be then given as

$$t_L = \left[\left(\frac{L}{\lambda}\right)^3 \frac{2\Lambda\nu\phi_\ell}{F_0k_\ell}\right]^{1/2}. \tag{9}$$

Because the plume buoyancy flux is independent of x, v_g and t_L are independent of H and, for that matter, Q_H and g'_H.

Note further that the height of the gravity current, $h(y,t)$, varies both in space and time. More precisely, $h(y,t)$ increases with t and decreases with $y\,(\le L_g)$. From figure 3 and (2.38) of Sahu and Flynn (2015), the mean gravity current height, $\bar{h}_{t_L}$, at $t = t_L$ can be calculated by averaging in y. Thus,

$$\bar{h}_{t_L} = \frac{1}{L}\int_0^L h(y,t=t_L)\,\mathrm{d}y = \frac{1}{\lambda}\left(\frac{\nu Q_H^2 t_L}{4\Lambda^2\phi_\ell^2 k_\ell g'_H}\right)^{1/3}, \tag{10}$$

where, consistent with observations, we assume that $h(y,t=t_L) > 0$ for $y < L$. Because $\bar{h}_{t_L}$ separately depends on Q_H and g'_H, this mean height does depend on H, unlike v_g and t_L.

After reaching the sidewalls, the discharged dense fluid forms a deepening layer of contaminated fluid whose upper boundary, termed the first front by Baines and Turner (1969), begins advecting upwards. Relative to the rising first front, there appears a sudden decrease

of permeability at height $\bar{h} = H_\ell$, measured from the bottom of the tank. Consequently, the timescales associated with the motion of the first front need to be defined separately in the lower and upper layers.

In the lower layer, at $t = t_L$, the curvature of the first front is dictated by the shape of the gravity current. By extension, the initial mean elevation of the first front is given by (10). If t_{H_ℓ} is the time required for the first front to subsequently advect to the permeability jump, we then require a formula for the mean height, $\bar{h}$, of the first front over $t_L < t < t_L + t_{H_\ell}$. The expression in question reads

$$\bar{h} = H_\ell + x_u - \left[(H_\ell + x_u - \bar{h}_{t_L})^{3/4} - \frac{3}{4}\frac{(t-t_L)}{A}\left(\frac{16F_0 k_\ell \Lambda \alpha^{1/2}}{\pi \nu \phi_\ell^{3/2}}\right)^{1/2}\right]^{4/3} \tag{11}$$

c.f. section 2.3 of Sahu and Flynn (2015). This result is valid up to the point where $\bar{h} = H_\ell$ and shows the correct limiting behaviour as $t \to t_L$ whereby $\bar{h} = \bar{h}_{t_L}$ as specified in (10). In the above equation, $A = 2\Lambda L$ is the tank cross-sectional area.

As the first front rises, its curvature decreases, i.e. the first front becomes progressively more horizontal. This levelling process is accelerated close to the permeability jump due to the added flow resistance associated with advection through the upper layer. To a first approximation, we therefore assume that the first front is horizontal as it begins to advect through the upper layer. The strength of this approximation obviously improves with increasing H_ℓ and decreasing k_u/k_ℓ. When $t = t_L + t_{H_\ell}$, $\bar{h} = H_\ell$, and (11) therefore yields

$$t_{H_\ell} = \frac{4}{3}A\left(\frac{\pi \nu \phi_\ell^{3/2}}{16F_0 k_\ell \Lambda \alpha^{1/2}}\right)^{1/2}\left[(H_\ell + x_u - \bar{h}_{t_L})^{3/4} - x_u^{3/4}\right]. \tag{12}$$

By extension, the counterpart of (11) for the upper layer reads

$$\bar{h} = H + x_0 - \left[(H + x_0 - H_\ell)^{3/4} - \frac{3}{4}\frac{(t - t_L - t_{H_\ell})}{A}\left(\frac{16F_0 k_u \Lambda \alpha^{1/2}}{\pi \nu \phi_u^{3/2}}\right)^{1/2}\right]^{4/3}. \tag{13}$$

Equation (13) is valid for $t_L + t_{H_\ell} < t < t_L + t_{H_\ell} + t_{H_u}$ where

$$t_{H_u} = \frac{4}{3}A\left(\frac{\pi \nu \phi_u^{3/2}}{16F_0 k_u \Lambda \alpha^{1/2}}\right)^{1/2}\left[(H + x_0 - H_\ell)^{3/4} - x_0^{3/4}\right] \tag{14}$$

is the time required for the first front to advect over the vertical distance H_u. Thus the total time required for the first front to advect to the level of the source is $t_{H_\ell} + t_{H_u}$.

The variation of $\bar{h}$ vs. t is presented in figure 6 for various k_u/k_ℓ and H_u/H_ℓ. The curves of figure 6 show an obvious kink, which becomes more pronounced as k_u/k_ℓ decreases but vanishes in the limit $k_u/k_\ell \to 1$. This disappearance reflects the fact that the porous medium becomes uniform when $k_u/k_\ell \to 1$ to that the precise values of H_u and H_ℓ become irrelevant. Conversely, the kink reflects the sudden increase of volume flux experienced by the plume as it enters the lower layer, whose higher permeability allows the first front to advect upwards comparatively quickly. This effect can also be discerned from the t derivatives of (11) and (13).

For the purposes of further comparing the above results with the uniform porous medium case, let us now assume that the control volume consists of a uniform porous medium where

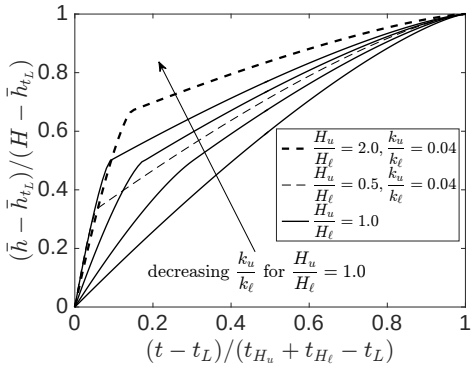

Fig. 6: Variation of $\bar{h}$ with time for various k_u/k_ℓ and H_u/H_ℓ (see equations 11–14). The values of k_u/k_ℓ for the solid lines decrease uniformly from 1.0 to 0.04. The bottom curve therefore indicates a uniform porous medium. The thick and thin dashed curves correspond to $k_u/k_\ell = 0.04$ with $H_u/H_\ell = 2.0$ and 0.5, respectively. Comparing these dashed curves against the top-most solid curve therefore shows the influence of H_u/H_ℓ.

the permeability and porosity are given by the following depth-weighted average values: $k_m = (H_u k_u + H_\ell k_\ell)/(H_u + H_\ell)$ and $\phi_m = (H_u\phi_u + H_\ell\phi_\ell)/(H_u + H_\ell)$. In this case, the time required for the gravity currents to reach the left and right sidewalls can be recovered from (9) by replacing k_ℓ and ϕ_ℓ by k_m and ϕ_m, respectively. Performing similar substitutions in (12), t_{H_m}, i.e. the time required for the first front to advect from the bottom to the top of the control volume, can be calculated. In this case, H_ℓ, x_u and $\bar{h}_{t_L}$ are replaced by H, x_m and $\bar{h}_{t_m}$, respectively, where, x_m and $\bar{h}_{t_L m}$ are the virtual source location and mean gravity current height for the uniform porous medium.

The dimensionless timescale associated with filling both the upper and lower layers can therefore be written as

$$t'_{\mathrm{A}} = \frac{t_L + t_{H_u} + t_{H_\ell}}{t_{L_m} + t_{H_m}}. \tag{15}$$

An equivalent expression for t'_{A} may be derived by neglecting the dynamics of the secondary gravity currents but assuming that the first front begins from the very bottom of the control volume. For further simplification, we also recall that the flow is in a Darcy regime and therefore assume either a weak non-ideal plume with $x_0 \ll H_u$ and $x_m \ll H$, or, alternatively, an ideal source with $x_0 = x_m = 0$. In either case, (6) shows that $x_u = \dfrac{\phi_u}{\phi_\ell}\left(\dfrac{k_u}{k_\ell}\right)^2 H_u$. On these bases, it can be shown that

$$t'_{\mathrm{A}} = \frac{\left(1+\frac{k_u}{k_\ell}\frac{H_u}{H_\ell}\right)^{1/2}\left\{\left(\frac{\phi_u}{\phi_\ell}\frac{H_u}{H_\ell}\right)^{3/4} + \left(\frac{k_u}{k_\ell}\right)^{1/2}\left[\left(1+\frac{\phi_u}{\phi_\ell}\left(\frac{k_u}{k_\ell}\right)^2\frac{H_u}{H_\ell}\right)^{3/4} - \left(\frac{\phi_u}{\phi_\ell}\left(\frac{k_u}{k_\ell}\right)^2\frac{H_u}{H_\ell}\right)^{3/4}\right]\right\}}{\left(\frac{k_u}{k_\ell}\right)^{1/2}\left(1+\frac{H_u}{H_\ell}\right)^{1/2}\left(1+\frac{\phi_u}{\phi_\ell}\frac{H_u}{H_\ell}\right)^{3/4}}. \tag{16}$$

The variation of t'_{A} with $k_u/k_\ell\,(<1)$ for various H_u/H_ℓ is shown in figure 7 a. Because $\phi_u/\phi_\ell = 1$, by assumption, $t'_{\mathrm{A}} = 1$ for all values of H_u/H_ℓ when $k_u/k_\ell = 1$ such that there is no difference between the lower and upper layers. Moreover, t'_{A} increases as k_u/k_ℓ decreases:

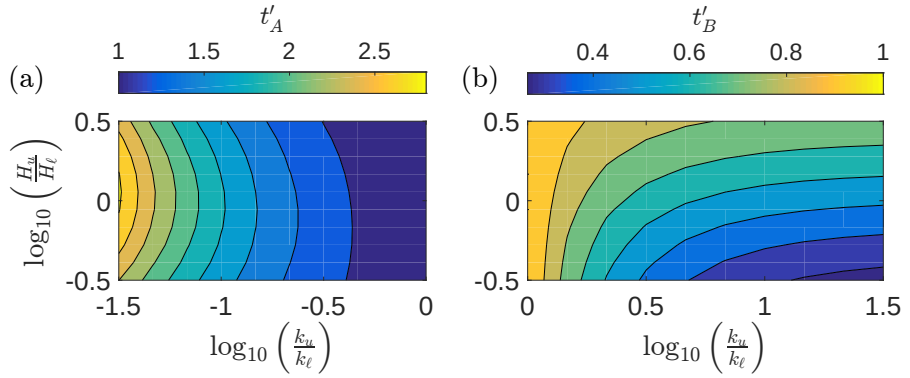

Fig. 7: [Color online] (a) Variation of t'_{A} with k_u/k_ℓ and H_u/H_ℓ based on (16). (b) Variation of t'_{B} with k_u/k_ℓ and H_u/H_ℓ based on (27) and (29). In both cases, $\phi_u/\phi_\ell = 1$. Note the difference of x-axis limits for panels a and b.

when $k_u/k_\ell < 1$, (4) shows that the plume volume flux remains very small throughout the upper layer. This has the effect of increasing t_{H_u} significantly as compared to the case where the upper layer permeability is $k_m\,(> k_u)$. The behaviour is consistent with the time-scales presented in figure 6 for $H_u/H_\ell = 1$, whereby $t_{H_u} \gg t_{H_\ell}$ when $k_u/k_\ell \ll 1$. Note, moreover, that the contours of figure 7 a show a peak when the upper and lower layers are equal in depth. As H_u/H_ℓ decreases from unity, the upper layer becomes thinner such that its influence on $t_{H_u} + t_{H_\ell}$ decreases, which further suggests that $t'_{\mathrm{A}} \approx 1$ as $H_u/H_\ell \to 0$. On the other hand, for $H_u/H_\ell > 1$ the difference between k_u and k_m decreases as does t'_{A}, which again approaches unity as H_u/H_ℓ now approaches infinity.

3.2 Permeability ratio $k_u/k_\ell > 1$

As discussed in section 2.2.2, when the permeability of the lower layer is comparatively small, the plume fluid discharged at the permeability jump takes the form of a porous media gravity current flowing over a porous base having an even lower permeability. While Huppert & Woods's solution has already been used to good effect in section 3.1, we adopt a methodology similar to that of Goda and Sato (2011) in approaching the current problem. Two important differences between our work and theirs are that (i) we consider miscible, not immiscible, fluids, and (ii) our control volume has closed boundaries whereas their two-layer porous medium was infinite in extent.

By assuming a hydrostatic pressure distribution, the governing equation for the primary gravity current height, $h_g(y,t)$, measured relative to the elevation of the permeability jump reads

$$\phi_u \frac{\partial h_g}{\partial t} = \frac{k_u g'_u}{\nu} \frac{\partial}{\partial y}\left(h_g \frac{\partial h_g}{\partial y}\right) - w. \tag{17}$$

Here $w = w(y,t)$ is the drainage velocity, whose value depends both on the primary gravity current height and the draining fluid depth $b(y,t)$ such that

$$w = \phi_\ell \frac{\partial b}{\partial t} = \frac{k_\ell}{\nu}\left(\frac{\bar{g}'_\ell b + g'_u h_g}{b}\right) = \frac{k_\ell \bar{g}'_\ell}{\nu}\left(1 + \frac{g'_u}{\bar{g}'_\ell}\frac{h_g}{b}\right). \tag{18}$$

The final two terms above come from combining Darcy's law, the hydrostatic pressure condition and the assumption that the flow in the lower layer is vertical (Pritchard et al, 2001; Goda and Sato, 2011). Moreover, g'_u and $\bar{g}'_\ell$ are the mean reduced gravities of the gravity current and of the draining fluid, respectively. The former parameter is easy to estimate based on the plume density at the level of the permeability jump. On the other hand, figure 4 suggests that $\bar{g}'_\ell < \bar{g}'_u$ on account of mixing. Because computing $\bar{g}'_\ell$ analytically is outside the scope of the current project, we shall later adopt an empirical approach that incorporates laboratory measurements – see section 4 and Appendix B.

Equations (17) and (18) are subject to the following boundary conditions

$$\frac{k_u g'_u}{\nu} h_g(0,t) \frac{\partial h_g(0,t)}{\partial y} = -\frac{Q_u}{2\Lambda}, \qquad \frac{k_u g'_u}{\nu} h_g(L_g(t),t) \frac{\partial h_g(L_g(t),t)}{\partial y} = 0,$$
$$h_g(L_g(t),t) = b(L_g(t),t) = 0. \tag{19}$$

Here $Q_u/2\Lambda$ is the plume volume flux per unit length at the permeability jump. Furthermore, h_g and b must also satisfy an expression of solute mass conservation such that

$$\int_0^{L_g(t)} \left[\phi_u h_g(y,t) + \frac{\bar{g}'_\ell}{g'_u} \phi_\ell b(y,t) \right] \mathrm{d}y = \frac{Q_u}{2\Lambda} t. \tag{20}$$

c.f. (2.25) and (3.21 b) of Sahu and Flynn (2015). Consistent with the previous discussion, but in contrast to section 3.1, we now assume that $t = 0$ corresponds to the instant in time when the plume first reaches the permeability jump.

As b progressively increases, the primary gravity current stops moving forward as the influx of dense plume fluid becomes balanced by fluid draining from the gravity current underside. In other words, and as time progresses, $\dfrac{h_g}{b}$ becomes small and $L_g(t) \to \check{L}_g$, where $\check{L}_g$ is the run-out length defined such that

$$\frac{Q_u}{2\Lambda} = \check{L}_g w \quad \Rightarrow \quad \check{L}_g = \frac{Q_u \nu}{2\Lambda k_\ell \bar{g}'_\ell}. \tag{21}$$

The run-out length for an immiscible system is defined by (1), which differs from (21) only with reference to the reduced gravity term ($\bar{g}'_\ell$ vs. g'_u). With the help of (4) and (21) it is now also possible to define a critical permeability ratio below which $\check{L}_g < L$, i.e.

$$\left(\frac{k_u}{k_\ell} \right)_{\text{crit}} = \frac{\pi \bar{g}'_\ell}{8 g'_u} \frac{L}{[\alpha \phi_u (H_u + x_0)]^{1/2}}. \tag{22}$$

When k_u/k_ℓ exceeds $(k_u/k_\ell)_{\text{crit}}$, the interfacial gravity current is predicted to collide with the lateral sidewalls.

As $L_g(t) \to \check{L}_g$, the gravity current height profile becomes independent of time. Thus, by combining (17), (18) and (19), it can ultimately be shown that

$$\check{h}_g = \left(\frac{k_\ell}{k_u} \frac{\bar{g}'_\ell}{g'_u} \right)^{1/2} (\check{L}_g - y) \quad \Rightarrow \quad \breve{h}_g = \left(\frac{k_\ell}{k_u} \frac{\bar{g}'_\ell}{g'_u} \right)^{1/2} \frac{\check{L}_g}{2}. \tag{23}$$

Here $\breve{h}_g$ is the mean gravity current height associated with a run-out length $\check{L}_g$. The linear form of the height profile obtained in (23) is similar to that obtained by Goda and Sato (2011) for immiscible fluids in a similar geometry. By contrast in the more complicated three-layer case where an upper layer with large k overlies both a thin bed with small k and

another deeper layer with large k, the height profile is known to be parabolic (Pritchard et al, 2001).

Corresponding to $\breve{\breve{h}}_g$, one can also derive an expression for the mean depth of the draining fluid. Indeed, and once the primary gravity current has stopped advancing, it can be shown that

$$\bar{b} = \frac{Q_u t}{2\Lambda\phi_\ell \breve{L}_g} - \frac{\phi_u}{\phi_\ell}\breve{\breve{h}}_g\,, \tag{24}$$

where the latter term incorporates the asymptotic mean depth of the primary gravity current. By setting $\bar{b} = H_\ell$ in (24) the time, t_{B_1}, required by the draining fluid to reach the bottom impermeable boundary can be estimated. Assuming $H_\ell \gg \breve{\breve{h}}_g$, the formula in question reads

$$t_{\mathrm{B}_1} = \frac{2\phi_\ell\Lambda\breve{L}_g H_\ell}{Q_u}\frac{\bar{g}'_\ell}{g'_u}\,. \tag{25}$$

Thereafter, a secondary gravity current is formed that fills, from the bottom up, the lower layer with contaminated fluid. Assuming a sharp interface between this contaminated fluid and the overlying ambient, we can infer the time, t_{B_2}, required to fill the remainder of the lower layer with discharged plume fluid from

$$t_{\mathrm{B}_2} = \frac{2\phi_\ell\Lambda H_\ell(L-\breve{L}_g)}{Q_u}\,. \tag{26}$$

The total time required to fill the lower layer can then be approximated as $t_{\mathrm{B}_1} + t_{\mathrm{B}_2}$.

After filling the lower layer, the interface between the dense and ambient fluids is assumed to advect upwards in the form of a first front as shown in figure 5 c. We proceed by considering a mean first front height, $\bar{h}$, as defined in (13). Equation (14) can then be used to estimate the time, t_{H_u}, required to fill the upper layer. Finally the total filling box time for this configuration with $k_u/k_\ell > 1$ is given by $t_{\mathrm{B}_1} + t_{\mathrm{B}_2} + t_{H_u}$.

To find a dimensionless time similar to that given by (16), we take the ratio of $t_{\mathrm{B}_1} + t_{\mathrm{B}_2} + t_{H_u}$ and t_{H_m}. After some simplification, it can be shown that

$$t'_{\mathrm{B}} = \frac{\left(1+\frac{k_u}{k_\ell}\frac{H_u}{H_\ell}\right)\left(\frac{\phi_u}{\phi_\ell}\frac{H_u}{H_\ell}+\frac{3}{4}\gamma\right)}{\frac{k_u}{k_\ell}\left(\frac{\phi_u}{\phi_\ell}\right)^{1/4}\left(1+\frac{\phi_u}{\phi_\ell}\frac{H_u}{H_\ell}\right)^{3/4}\left(\frac{H_u}{H_\ell}\right)^{3/4}\left(1+\frac{H_u}{H_\ell}\right)^{1/2}}\,, \tag{27}$$

in which the non-dimensional parameter γ is defined by

$$\gamma = 1 - \frac{\breve{L}_g}{L}\left(1-\frac{\bar{g}'_\ell}{g'_u}\right) = 1 - \frac{Q_u\nu}{2\Lambda L k_\ell \bar{g}'_\ell}\left(1-\frac{\bar{g}'_\ell}{g'_u}\right)\,, \tag{28}$$

where (21) has been applied in the latter equality. Because $0 < \bar{g}'_\ell/g'_u \leq 1$ and (27) is valid only when $L_g \leq L$, $0 < \gamma \leq 1$. In an immiscible system where $\bar{g}'_\ell/g'_u = 1$, $\gamma = 1$. On the other hand, for a miscible system, we cannot estimate γ precisely without knowing the details of the mixing that occurs within the lower layer. Fortunately, we will show below that even bracketing γ between zero and unity provides meaningful bounds on the range of possible solutions. Note finally that γ is expected to vary with H_u/H_ℓ, k_u/k_ℓ and ϕ_u/ϕ_ℓ. Although the variation of γ with the latter two ratios is difficult to discern theoretically, we can gain some insight into the variation of γ with H_u/H_ℓ by considering the limits $k_u/k_\ell \to 1$ and

Expt no.	H_u (cm)	Q_0 (cm^3/s)	g_0' (cm/s^2)	$\check{L}_g/L$	$\check{L}_{g,\ell}/L$	$\check{L}_{g,u}/L$
9	12.0	0.30	29.43	0.223	0.186	0.248
10	12.0	0.80	29.43	0.233	0.335	0.471
11	12.0	0.30	78.48	0.221	0.231	0.233
12	12.0	0.80	78.48	0.223	0.295	0.366
32	20.0	0.25	21.20	0.288	0.241	0.422
33	20.0	0.75	21.20	0.310	0.402	0.646
34	20.0	0.25	82.40	0.286	0.228	0.281
35	20.0	0.75	82.40	0.286	0.241	0.385

Table 1: Primary gravity current run-out lengths for various H_u/H_ℓ, Q_0 and g_0' and $k_u/k_\ell = 9.0$. The prediction, $\check{L}_g$ is obtained from (21). Moreover, $\check{L}_{g,\ell}$ and $\check{L}_{g,u}$ are measured using HTS images and derived from horizontal line segments located at $x = H_u + h_\ell/2$ (figure 5 e) and $x = H_u^-$ (figure 5 d), respectively. Further experimental parameters are specified in tables 2 and 3, Appendix A.

$\phi_u/\phi_\ell \to 1$ in (27) whereby we expect $t_{\rm B}'$ to approach unity. On this basis, it can be shown that

$$\gamma = \frac{4H_u}{3H_\ell}\left[\left(1+\frac{H_\ell}{H_u}\right)^{1/4} - 1\right], \tag{29}$$

i.e. γ is predicted to increase with H_u/H_ℓ. Because it is unclear how to extend (29) to $k_u/k_\ell > 1$, we present in figure 7 b solutions for $t_{\rm B}'$ derived by combining (27) and (29). Obviously, the results shown in figure 7 b must be interpreted with some care; nonetheless, they suggest that $t_{\rm B}'$ decreases with increasing k_u/k_ℓ and decreasing H_u/H_ℓ.

4 Comparison between theory and experiment

Figure 8 shows the mean elevation, $\bar{h}$, of the first front vs. time for various $k_u/k_\ell < 1$. The figure considers the case of equal upper and lower layer depths; similar results (not shown) apply when $H_u/H_\ell \neq 1$. Model predictions are verified using experimental data corresponding to different source conditions: generally good agreement is observed in all cases. More specifically, the experimental data capture the sudden change of slope experienced when the first front reaches the permeability jump; this effect is obviously more pronounced for smaller k_u/k_ℓ. Comparing panels (a) and (c), in particular the horizontal coordinate of the kink, also confirms that as k_u/k_ℓ decreases, the fraction of time required to fill the upper layer increases significantly for fixed height ratio.

When $k_u/k_\ell > 1$, a well-defined first front does not exist in the lower layer (see figure 3). However, because gravity currents are generated at the permeability jump, we can compare measured run-out lengths with the analogue predictions due to (21). Such a comparison is made in table 1. The reduced gravity, $\bar{g}_\ell'$, of the draining fluid in (21) is obtained empirically and equals $\bar{g}_\ell' = (0.6 \pm 0.1)\, g_u'$ (see Appendix B), where g_u' is estimated from (4). Table 1 is limited to eight entries, all with $k_u/k_\ell = 9.0$: when $k_u/k_\ell = 2.8$, $\check{L}_g/L \ll 1$ and when $k_u/k_\ell = 25.0$ (or when $k_u/k_\ell = 9.0$ but $H_u/H_\ell = 2.0$), $\check{L}_g/L > 1$ – see figures 3 d,f. In the former (latter) case, measurements of $\check{L}_g$ are problematic (impossible), and hence any comparison with the predictions of section 3 is not worthwhile. On the other hand, when $k_u/k_\ell = 9.0$ and $H_u/H_\ell = 0.5$ or 1.0, $\mathcal{O}(0.1) < \check{L}_g/L < 1$, and it is therefore possible to make a comparison with theory. In drawing such a comparison, note that figures 5 d and 5 e

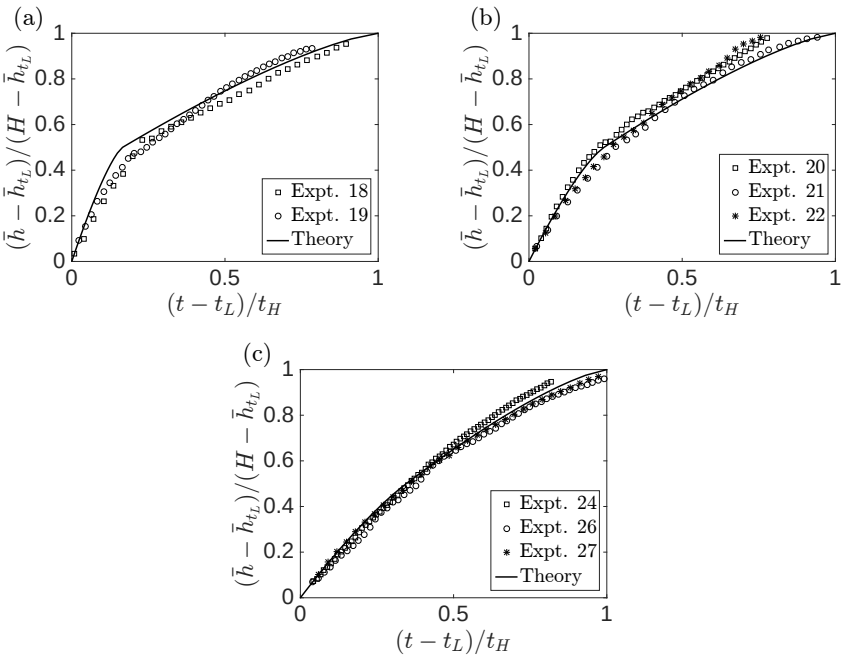

Fig. 8: First front mean elevation when (a) $k_u/k_\ell = 0.04$, (b) $k_u/k_\ell = 0.11$ and (c) $k_u/k_\ell = 0.36$. Experimental parameters are specified in table 3, Appendix A. Note that $H_u/H_\ell = \phi_u/\phi_\ell = 1.0$ in all cases.

show two different experimental values, one measured immediately above the permeability jump and one measured below, i.e. midway between the permeability jump and the lower boundary. However, recall from (21) that $\check{L}_g$ is predicted by balancing the plume volume flux, $Q_u/2\Lambda$, with the flux of dense fluid draining into the lower layer from the gravity current underside. Figure 5 a suggests that this draining volume flux is more properly associated with a run-out length measured below ($\check{L}_{g,\ell}$), not above ($\check{L}_{g,u}$), the permeability jump. On this basis, it is more appropriate to compare $\check{L}_g$ with $\check{L}_{g,\ell}$.

From table 1 we find that the comparison between the predicted ($\check{L}_g$) and measured ($\check{L}_{g,\ell}$) values for the run-out length is reasonable; for the data set as a whole, the standard deviation for $\check{L}_g - \check{L}_{g,\ell}$ is $\pm 23\%$. The likely reasons for this discrepancy are as follows: (i) The parameterization $\bar{g}'_\ell/g'_u = 0.6 \pm 0.1$ reflects the mean of 14 experiments conducted with fixed lower layer depth. (ii) In contrast to sharp interface models, the front between the contaminated and ambient fluids actually appears diffuse as a result of dispersion and light scattering effects. It is therefore difficult to experimentally measure the run-out length (whether above or below the permeability jump) with great precision.

In order to explore the variation of the filling box time with k_u/k_ℓ, results are plotted in figure 9 for all 50 experiments where panels (a), (b) and (c) correspond, respectively, to $H_u/H_\ell = 0.5$, 1.0 and 2.0. The experimental data are corrected for finite source effects by adding the time required for the first front to advect from $x = 0$ to $x = -x_0$. Recall that the filling box time is denoted by t'_{A} when $k_u/k_\ell \leq 1$ (see equation 16) and by t'_{B} when $k_u/k_\ell > 1$ (see equation 27). Because t'_{B} depends on γ where $0 < \gamma \leq 1$, the corresponding prediction is

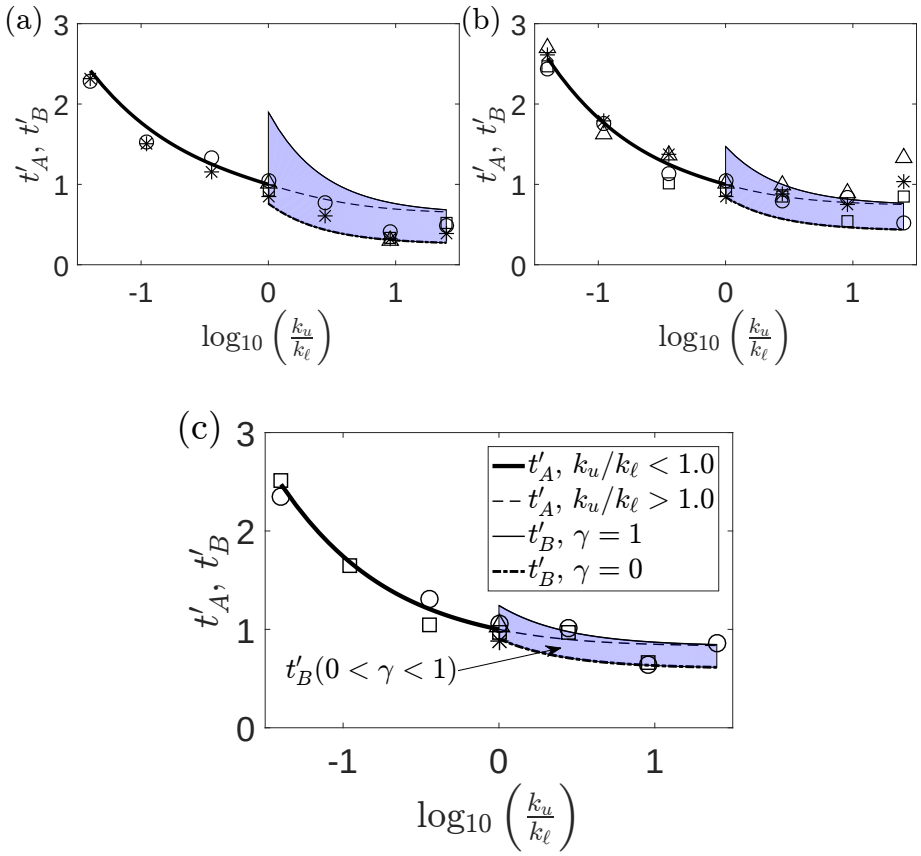

Fig. 9: [Color online] Non-dimensional filling box time for $\phi_u/\phi_\ell = 1$ and (a) $H_u/H_\ell = 0.5$, (b) $H_u/H_\ell = 1.0$ and (c) $H_u/H_\ell = 2.0$. Discrete data show the measured values; the data presented for $k_u/k_\ell = 1.0$ correspond to Experiments 1, 3, 7 and 8 of Sahu & Flynn (Sahu and Flynn, 2015, table 1). Symbols correspond to the following ranges of values for Q_0 and g'_0: (i) circles: $0.20 \le Q_0 \le 0.50$ (cm^3/s), $25.0 \le g'_0 \le 50.0$ (cm/s^2), (ii) stars: $0.60 \le Q_0 \le 0.80$ (cm^3/s), $25.0 \le g'_0 \le 50.0$ (cm/s^2), (iii) squares: $0.20 \le Q_0 \le 0.50$ (cm^3/s), $60.0 \le g'_0 \le 80.0$ (cm/s^2) and (iv) triangles: $0.60 \le Q_0 \le 0.80$ (cm^3/s), $60.0 \le g'_0 \le 80.0$ (cm/s^2).

shown not by a single curve but rather using a shaded region covering all permissible values of γ. Note that this shaded region becomes shorter with decreasing H_ℓ in which case there less opportunity for mixing between lower layer ambient fluid and the contaminated fluid that drains from the primary gravity current.

Although $t'_{\rm A}$ was derived by assuming $k_u/k_\ell \le 1.0$, in figure 9 we extend the (thick) curve in question into the right half plane to examine its efficacy for $k_u/k_\ell > 1$. This extension implies, in effect, that whatever entrainment may be associated with contaminated fluid draining from the underside of the primary gravity current is comparable to that associated

with a single descending plume. Note, in particular, that the extended portion of the curve overlaps with the $\gamma = 1$ limit of (27) for $k_u/k_\ell \gg 1$.

On comparing theory and experiment in figure 9 with $k_u/k_\ell < 1$, we generally find good agreement between measured data points and the thick solid curve. When $k_u/k_\ell > 1.0$, the experimental values almost always fall within the shaded region except in panel (b) when $k_u/k_\ell = 25.0$. The scatter of data in this latter case is primarily because $\check{L}_g/L > 1$. The lower layer therefore becomes isolated as in figure 3 f, whereby the upper layer fills faster than the lower layer and it becomes difficult to ascertain when the entire control volume has become filled with contaminated fluid. There are, in other words, additional physical effects at play that are not thoroughly accounted for by (27). Further examination of these effects, e.g. mixing by Rayleigh-Taylor-type instabilities (Homsy, 1987; Drazin and Reid, 2004) in porous media flow, shall be the topic of future investigations.

5 Conclusions

Porous media filling box flows are studied experimentally and analytically to examine the effects of sudden permeability changes in a rectilinear control volume. The flow is assumed to be Boussinesq and laminar such that the Pe $\gg \mathcal{O}(1)$ where Pe is the Péclet number. The buoyant convection is driven by a line source that spans the width of the control volume and whose effluent is miscible within the ambient fluid that saturates the porous medium.

Experiments were performed considering as independent variables the permeability (k_u/k_ℓ) and height (H_u/H_ℓ) ratios of the upper and lower layers as well as the source volume flux (Q_0) and reduced gravity (g_0'). When $k_u/k_\ell < 1.0$, the observed flow dynamics are qualitatively similar to the case of a uniform porous medium, i.e. when $k_u/k_\ell = 1$. The flow is then characterized by (i) a negatively-buoyant plume, (ii) oppositely-directed gravity currents that propagate along the lower impermeable boundary and (iii) a first front that propagates in the vertical direction towards the source. Accordingly the analytical formulations of Sahu and Flynn (2015) are adopted when predicting key dynamical parameters e.g. the time-scales associated with the motion of the gravity currents and first front. In the present case, however, different permeabilities and virtual source corrections must be applied for the upper and lower layers.

On the other hand, the experiments with $k_u/k_\ell > 1.0$ exhibit qualitatively different flow dynamics from those relevant to the uniform porous medium case. After reaching the permeability jump, the dense plume divides into two parts. Some of the plume fluid propagates horizontally outward as a pair of oppositely-directed (primary) gravity currents. The remaining fraction of the plume fluid directly drains into the lower layer and subsequently creates a pair of (secondary) gravity currents that propagate along the lower impermeable boundary. The flow of the primary and secondary gravity currents are distinct one from the other. Because of continuous drainage from the underside of the primary gravity current, the motion of the front is irregular, i.e. the front temporarily stops after traveling a finite horizontal distance that decreases with g_0' but increases with k_u/k_ℓ and Q_0. Therefore, in several cases, for instance the experiments with $k_u/k_\ell = 25.0$, $\check{L}_g > L$, where L is the horizontal distance of the sidewall from the source. In such instances, the ambient fluid in the lower layer becomes isolated from that in the upper layer. Consequently, only a relatively small volume of discharged plume fluid may infiltrate the lower layer by the time of overflow, defined as the time at which discharged plume fluid reaches the elevation of the source in the upper layer. A formula for $\check{L}_g$ is presented in (21), which allows for mixing between the draining fluid and the lower layer ambient fluid. Although it is outside of the scope of the present inquiry to

analytically estimate the degree of mixing, e.g. as a function of k_u/k_ℓ, Appendix B presents a methodology by which such estimates may be made experimentally. Accordingly, and for $k_u/k_\ell = 9.0$, we find that $\bar{g}'_\ell = (0.6 \pm 0.1)\, g'_u$ where $\bar{g}'_\ell$ and g'_u are the reduced gravities of the draining fluid and the primary gravity current, respectively.

For $k_u/k_\ell < 1.0$, the filling box time, $t'_{\rm A}$, is given by (16). The corresponding time, $t'_{\rm B}$, for the $k_u/k_\ell > 1.0$ case is given by (27). Except when $\check{L}_g/L > 1.0$, generally good agreement is noted between predictions and measurements of $t'_{\rm A}$ and $t'_{\rm B}$ (figure 9).

An important limiting assumption of the present work is that it assumes a horizontal permeability jump between the upper and lower layers. However, in real geophysical scenarios, thrust may render such permeability jumps non-horizontal and even non-planar. In the near future, we therefore plan to study the effects of inclined porous layers in the context of filling box flows.

Acknowledgments

The current research is supported by NSERC (Discovery Grant and RTI programmes) and Carbon Management Canada. The authors wish to acknowledge the contribution of Johny Jose, an intern from IIT Kharagpur, who assisted with the collection of some of the experimental data. The authors also acknowledge the kind assistance provided by Mitch Nicholson in writing the algorithms used to construct HTS and CTS images of the type shown in figure 5. Experiments were conducted in the laboratory of Dr. Bruce R. Sutherland whose loan of space and equipment is acknowledged with gratitude.

A Experimental details

Tables 2, 3 and 4 specify the parameters for the 50 experiments described in section 2.1. These experiments were performed for the purposes of analysing and quantifying the flow behaviour both when $k_u/k_\ell < 1.0$ and $k_u/k_\ell > 1.0$. On the contrary, the experiments listed in table 5, Appendix B were performed only for the purpose of estimating $\bar{g}'_\ell/g'_u$. These are discussed in the next section along with an explanation of the corresponding experimental technique.

B Determination of the reduced gravity, $\bar{g}'_\ell$, of the draining fluid

Here we outline experiments and a Matlab-based post-processing algorithm for determining the relationship between $\bar{g}'_\ell$ and g'_u, specifically for the permeability ratio $k_u/k_\ell = 9.0$. This information is, in turn, needed when calculating the run-out length as we do in table 1. For simplicity, the present experiments consider $H_u/H_\ell = 1$ with $H_\ell \simeq 19$ cm. For the data reported below, we expect only very minor quantitative differences for moderately larger H_ℓ e.g. $H_\ell = 20$ cm ($H_u = 20$ cm in table 1) or $H_u = 24$ cm ($H_u = 12$ cm in table 1). These differences would, in our estimation, fall within the error estimates due to measurement errors. Note also that the methodology described below is loosely based on Dong and Selvadurai (2006), whose analysis guides the present formulation.

First, we ran a series of calibration experiments, which were conducted in order to find a correlation between the concentration of Procion MX Cold Water dye and the average pixel intensity within two interrogation windows, one above the permeability jump and the other below. Thus, the entirety of the experimental tank was filled with dyed water having the same uniform dye concentration after which experimental images were recorded using the Canon Rebel T2i camera. Although the dye concentration was uniform, the pixel intensity was not: the lower layer generally appeared to be much darker on account of the smaller bead diameter i.e. 1 mm vs. 3 mm. Calibration experiments were conducted for eight different dye concentrations in the range $0 - 0.18$ g/L; dye concentrations were therefore deliberately depressed relative to the experiments described in Appendix A. On the basis of the images collected from these eight experiments, calibration curves were then generated which yielded the variation of image intensity as a function of dye concentration for both the upper and lower layers.

Expt no.	d_1 (cm)	d_2 (cm)	k_u ($\times 10^{-5}$ cm^2)	k_ℓ ($\times 10^{-5}$ cm^2)	k_u/k_ℓ	Q_0 (cm^3 s^{-1})	g_0' (cm s^{-2})
1	0.1	0.5	0.87	21.80	0.04	0.30	29.43
2	0.1	0.5	0.87	21.80	0.04	0.80	29.43
3	0.1	0.3	0.87	7.84	0.11	0.30	29.43
4	0.1	0.3	0.87	7.84	0.11	0.80	29.43
5	0.3	0.5	7.84	21.80	0.36	0.30	29.43
6	0.3	0.5	7.84	21.80	0.36	0.80	29.43
7	0.5	0.3	21.80	7.84	2.8	0.30	29.43
8	0.5	0.3	21.80	7.84	2.8	0.80	29.43
9	0.3	0.1	7.84	0.87	9.0	0.30	29.43
10	0.3	0.1	7.84	0.87	9.0	0.80	29.43
11	0.3	0.1	7.84	0.87	9.0	0.30	78.48
12	0.3	0.1	7.84	0.87	9.0	0.80	78.48
13	0.5	0.1	21.80	0.87	25.0	0.30	29.43
14	0.5	0.1	21.80	0.87	25.0	0.80	29.43
15	0.5	0.1	21.80	0.87	25.0	0.30	78.48

Table 2: Summary of the experimental parameters for the cases where $H_u/H_\ell = 0.5$. Here d_1 and d_2 respectively denote the bead diameters of the upper and lower layers. Moreover, k_u and k_ℓ respectively denote the permeabilities of the upper and lower layers. Finally, Q_0 and g_0' are the source volume flux and reduced gravity. Note that $\phi_u/\phi_\ell = 1.0$ in all cases.

Expt no.	d_1 (cm)	d_2 (cm)	k_u ($\times 10^{-5}$ cm^2)	k_ℓ ($\times 10^{-5}$ cm^2)	k_u/k_ℓ	Q_0 (cm^3 s^{-1})	g_0' (cm s^{-2})
16	0.1	0.5	0.87	21.80	0.04	0.30	29.43
17	0.1	0.5	0.87	21.80	0.04	0.75	29.43
18	0.1	0.5	0.87	21.80	0.04	0.30	78.48
19	0.1	0.5	0.87	21.80	0.04	0.75	78.48
20	0.1	0.3	0.87	7.84	0.11	0.30	29.43
21	0.1	0.3	0.87	7.84	0.11	0.30	78.48
22	0.1	0.3	0.87	7.84	0.11	0.75	78.48
23	0.1	0.3	0.87	7.84	0.11	0.30	48.07
24	0.3	0.5	7.84	85.35	0.36	0.30	29.43
25	0.3	0.5	7.84	21.09	0.36	0.80	29.43
26	0.3	0.5	7.84	21.09	0.36	0.30	78.48
27	0.3	0.5	7.84	21.09	0.36	0.80	78.48
28	0.5	0.3	21.80	7.84	2.8	0.30	31.39
29	0.5	0.3	21.80	7.84	2.8	0.80	31.39
30	0.5	0.3	21.80	7.84	2.8	0.30	77.49
31	0.5	0.3	21.80	7.84	2.8	0.75	77.49
32	0.3	0.1	21.80	0.87	9.0	0.25	21.20
33	0.3	0.1	21.80	0.87	9.0	0.75	21.20
34	0.3	0.1	21.80	0.87	9.0	0.25	82.40
35	0.3	0.1	21.80	0.87	9.0	0.75	82.40
36	0.3	0.1	7.84	0.87	9.0	0.30	48.07
37	0.5	0.1	7.84	0.87	25.0	0.30	17.16
38	0.5	0.1	7.84	0.87	25.0	0.30	31.39
39	0.5	0.1	7.84	0.87	25.0	0.80	31.39
40	0.5	0.1	7.84	0.87	25.0	0.80	81.42

Table 3: As in table 2 but with $H_u/H_\ell = 1.0$.

Expt no.	d_1 (cm)	d_2 (cm)	k_u ($\times 10^{-5}$ cm^2)	k_ℓ ($\times 10^{-5}$ cm^2)	k_u/k_ℓ	Q_0 (cm^3 s^{-1})	g_0' (cm s^{-2})
41	0.1	0.5	0.87	21.80	0.04	0.30	23.43
42	0.1	0.5	0.87	21.80	0.04	0.40	23.43
43	0.1	0.3	0.87	7.84	0.11	0.70	43.16
44	0.3	0.5	7.84	21.80	0.36	0.30	29.43
45	0.3	0.5	7.84	21.80	0.36	0.80	29.43
46	0.5	0.3	21.80	7.84	2.8	0.30	43.16
47	0.5	0.3	21.80	7.84	2.8	0.70	43.16
48	0.3	0.1	7.84	0.87	9.0	0.25	43.16
49	0.3	0.1	7.84	0.87	9.0	0.50	43.16
50	0.5	0.1	21.09	7.84	25.0	0.25	43.16

Table 4: As in table 2 but with $H_u/H_\ell = 2.0$.

Expt no.	Q_0 (cm^3)/s	g_0' (cm/s^2)	$\bar{g}_\ell'/g_u'$
51	0.25	22.1	0.58
52	0.50	22.1	0.55
53	0.80	22.1	0.53
54	0.52	34.8	0.52
55	0.67	34.8	0.67
56	0.81	34.8	0.52
57	0.32	54.9	0.66
58	0.50	54.9	0.56
59	0.62	54.9	0.46
60	0.81	54.9	0.58
61	0.30	77.1	0.76
62	0.45	75.5	0.74
63	0.63	75.5	0.76
64	0.77	77.1	0.60

Table 5: Experimental parameters for the experiments used to estimate $\bar{g}_\ell'/g_u'$ with $k_u/k_\ell = 9.0$.

With the above calibration data to hand, flow experiments were performed following the general methodology of section 2.1 and using the same background illumination and camera settings as with the calibration experiments. A total of 14 experiments were conducted where the source conditions were varied as follows: $0.20 \le Q_0 \le 0.80$ cm^3/s, $20.0 \le g_0' \le 80.0$ cm/s^2. In all 14 experiments, the primary gravity current reached its run-out length at or before the time, t_1, when contaminated fluid first reached the bottom boundary. Experimental images were recorded at t_1 and formed the basis for the image processing analysis to be described below.

For each experimental image, we returned to the same interrogation windows described previously. By computing the average intensities within these windows, and using the calibration curves, we could straightforwardly estimate the dye concentrations. Because our flow is characterized by large Péclet numbers, it was assumed that the solute concentrations varied in direct proportion to the dye concentrations. The lower layer to upper layer ratio of the latter therefore yielded the ratio of the solute concentrations. It was then easy to estimate the ratio, $\bar{g}_\ell'/g_u'$, of the average reduced gravity of the draining fluid to that of the primary gravity current. Note finally that by obtaining analytical values of g_u' from (4), a precise estimate for $\bar{g}_\ell'$ could then be obtained.

Table 5 gives a list of the experimental parameters for the 14 experiments in question along with the associated estimates for $\bar{g}_\ell'/g_u'$. The values of $\bar{g}_\ell'/g_u'$ varied in the range of $0.45-0.75$. From these 14 experiments, the mean value of $\bar{g}_\ell'/g_u'$ obtained was 0.6 with an error of 0.1, corresponding to the standard deviation of the data set. Furthermore, no systematic variation of $\bar{g}_\ell'/g_u'$ with the source parameters was found. We conclude therefore that $\bar{g}_\ell'/g_u' = 0.6 \pm 0.1$ is a meaningful average value, at least for the case where $k_\ell/k_u = 9.0$.

References

Acton JM, Huppert HE, Worster MG (2001) Two-dimensional viscous gravity currents flowing over a deep porous medium. J Fluid Mech 440:359–380

Baines WD, Turner JS (1969) Turbulent buoyant convection from a source in a confined region. J Fluid Mech 37:51–80

Chen KS, Ho JR (1986) Effect of flow inertia on vertical natural convection in saturated porous media. Int J Heat Mass Transfer 29:753–759

Delgado JMPQ (2007) Longitudinal and transverse dispersion in porous media. IChemE 85 (A9):1245–1252

Dong W, Selvadurai APS (2006) Image processing technique for determining the concentration of a chemical in a fluid-saturated porous medium. Geotech Test J 29-5:1–7

Drazin PG, Reid WH (2004) Hydrodynamic stability. Cambridge University press

Dudfield P, Woods AW (2012) On the periodic injection of fluid into, and its extraction from, a porous medium for seasonal heat storage. J Fluid Mech 707:467–481

Goda T, Sato K (2011) Gravity currents of carbon dioxide with residual gas trapping in a two-layered porous medium. J Fluid Mech 673:60–79

Happel J, Brenner H (1991) Low Reynolds Number Hydrodynamics: With Special Applications to Particulate Media, 2nd edn. Kluwer Academic

Homsy GM (1987) Viscous fingering in porous media. Ann Rev Fluid Mech 19:271–311

Huppert HE, Woods AW (1995) Gravity-driven flows in porous layers. J Fluid Mech 292:55–69

Huppert HE, Neufeld JA, Strandkvist S (2013) The competition between gravity and flow focusing in two-layered porous media. J Fluid Mech 720:5–14

Lai FC (1991) Non-darcy convection from a line source of heat in a saturated porous medium. Int Comm Heat Mass Transfer 18:445–457

Lyle S, Huppert HE, Hallworth M, Bickle M, Chadwick A (2005) Axisymmetric gravity currents in a porous medium. J Fluid Mech 543:293–302

Lyu X, Woods AW (2016) Experimental insights on the development of buoyant plumes injected into a porous media. Geophys Res Lett 43:709–718

Moradi A, Flynn MR (2017) Emptying filling boxes – free turbulent versus laminar porous media plumes. J Fluid Mech 817:490–513

Nicholson M, Flynn MR (2015) Gravity current flow over sinusoidal topography in a two-layer ambient. Phys Fluids 27:096,603, 1–20

Pritchard D, Hogg AJ (2002) Draining viscous gravity currents in a vertical fracture. J Fluid Mech 459:207–216

Pritchard D, Woods AW, Hogg AJ (2001) On the slow draining of a gravity current moving through a layered permeable medium. J Fluid Mech 444:23–47

Roes MA (2014) Buoyancy-driven convection in a ventilated porous medium. Master's thesis, University of Alberta

Roes MA, Bolster DT, Flynn MR (2014) Buoyant convection from a discrete source in a leaky porous medium. J Fluid Mech 755:204–229

Saffman PG, Taylor SG (1958) The penetration of fluid into a porous medium or hele-shaw cell containing a more viscous liquid. Proceedings of the Royal Society of London A:312–329

Sahu CK, Flynn MR (2015) Filling box flows in porous media. J Fluid Mech 782:455–478

Sahu CK, Flynn MR (2016) Filling box flows in an axisymmetric porous medium. Transp Porous Med 112:619–635

Schulze S, Nikrityuk PA, Meyer B (2015) Porosity distribution in monodisperse and polydisperse fixed beds and its impact on the fluid flow. Particulate Science and Technology 33:23–33

Shin JO, Dalziel SB, Linden PF (2004) Gravity currents produced by lock exchange. J Fluid Mech 521:1–34

Spannuth MJ, Neufeld JA, Wettlaufer JS, Worster MG (2009) Axisymmetric viscous gravity currents flowing over a porous medium. J Fluid Mech 622:135–144

Thomas LP, Marino BM, Linden PF (1998) Gravity currents over porous substrates. J Fluid Mech 366:239–258

Ungarish M, Huppert HE (2000) High-reynolds-number gravity currents over a porous boundary: shallow-water solutions and box-model approximations. J Fluid Mech 418:1–23

Wooding RA (1963) Convection in a saturated porous medium at large rayleigh number or péclet number. J Fluid Mech 15:527–544